ACS OMEGA

Open Access

http://pubs.acs.org/journal/acsodf

Article

Enabling the Ultraenrichment of Colloidal Particles via Continuous Droplet Manipulation

Tianyi Lu,[§] Miaoran Liu,[§] Yifei Xiao,[§] Yimeng Xu, Yu Wang, Ziyi Dai,* and Kai Qian*

Cite This: *ACS Omega* 2025, 10, 6038−6046

Read Online

ACCESS | Metrics & More | Article Recommendations | Supporting Information

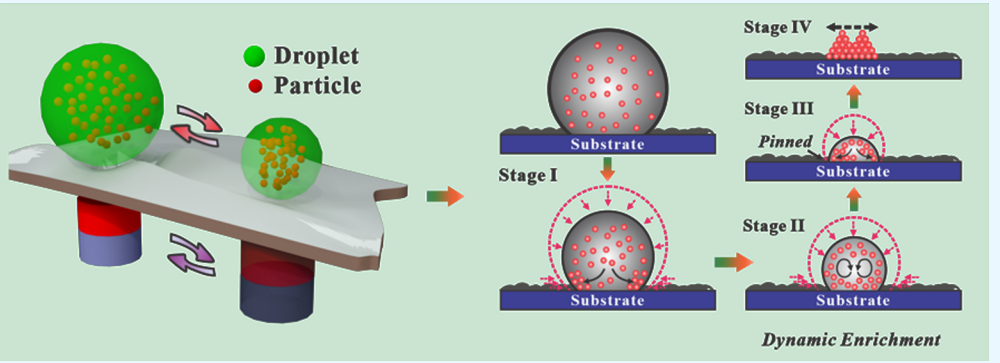

ABSTRACT: Concentration and uniform deposition of particles during droplet evaporation remain significant challenges in analytical systems. This natural and appropriate design of the processing steps can effectively bridge the gap between the low-concentration test substance and the accuracy of the test tool and therefore has attracted widespread academic and industrial attention. However, conventional static evaporation faces two major challenges: limited concentration efficiency and nonuniform particle deposition due to the coffee-ring effect. Here, we introduce a "dynamic enrichment" method based on a magnetically actuated droplet manipulation platform, which fundamentally alters the traditional static concentration process. This approach enables both superior enrichment and uniform particle distribution on superhydrophobic surfaces through controlled droplet movement. We systematically investigated the enrichment behavior using model particles of varying densities and sizes under different experimental conditions, including droplet volume and initial concentration. The method demonstrates consistent performance across these diverse particle properties, achieving a higher concentration efficiency and more uniform deposition compared to static enrichment. Through characterization and mechanistic statements, we show that this platform could potentially serve as a foundation for developing sensitive analytical techniques, particularly considering that the working range of particle properties aligns well with those of common biological and chemical analytes.

1. INTRODUCTION

In the realm of analytical chemistry, the effective concentration and uniform deposition of particles from evaporating droplets presents two significant technical challenges, including insufficient enrichment efficiency and the well-documented "coffee-ring effect."[1,2] These limitations are particularly evident in solid-phase detection methods, where conventional droplet evaporation patterns, especially for 10 μL droplets on hydrophilic surfaces, typically result in both diluted and nonuniform millimeter-scale diameter deposits. These phenomena substantially undermine the reliability of sample preparation, particularly in dealing with low-concentration analytes. The inherent limitations of current concentration methods necessitate additional processing steps, which not only escalate costs but also demand laborious and specialized handling. In light of these challenges, there emerges a pressing need to augment both the enrichment efficiency and the deposition uniformity of individual droplets.

In pursuit of advancing analyte detection at the droplet level, extensive research has been conducted with a focus on optimizing enrichment efficiency and uniformity.[3−5] The substrate's wettability plays a pivotal role in determining droplet concentration efficiency.[6] On hydrophilic surfaces, the polar groups exhibit a strong affinity for water, resulting in droplets with smaller contact angles and expansive contact lines. This facilitates the formation of a deposition pattern by dispersant molecules during evaporation, a pattern that diminishes as the hydrophobicity increases. Conversely, on

Received: November 7, 2024
Revised: January 20, 2025
Accepted: January 29, 2025
Published: February 7, 2025

https://doi.org/10.1021/acsomega.4c10019
ACS Omega 2025, 10, 6038−6046

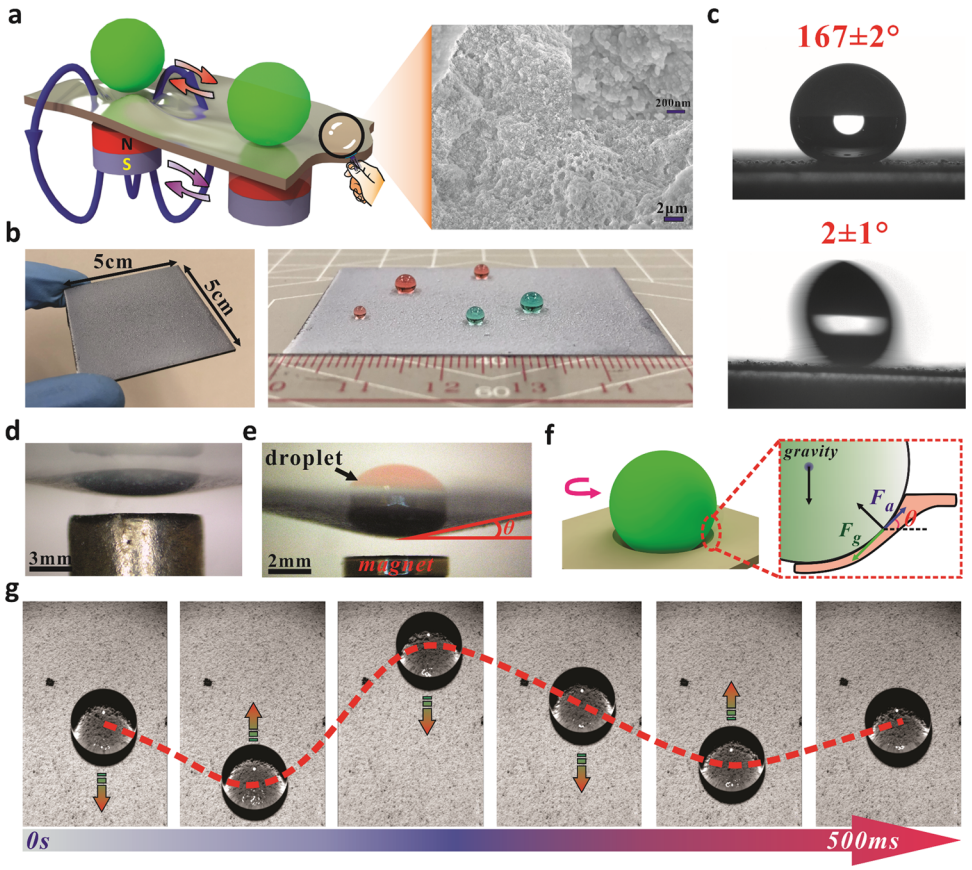

Figure 1. (a) Diagram of dynamic control and SEM image of superhydrophobic surfaces. (b) Optical image of the 5 cm × 5 cm magnetic-superhydrophobic surface and dyed droplets with different volumes. (c) Contact angle and sliding angle of the superhydrophobic surface. (d) The film fixed at a hollow glass substrate exhibits a concave shape under the applied force of cylindrical magnets. (e) Film with a 50 μL droplet on top and located at the dent. (f) Diagram of the force analysis of the droplet on the deformed film. (g) Optical image of movement of droplets (20 μL) on the superhydrophobic surface driven by the magnet in a period of 500 ms.

nonwetting surfaces, the droplet's three-phase contact line (TCL) tends to retract during enrichment, yielding a smaller, more desirable deposition pattern. The presence of micronano structures can extend the Cassie state, reducing the area fraction through additional air cavities and leading to subspherical droplets with highly enriched patterns.[7] Theoretically, contact angles approaching 180° could maximize enrichment efficiency. However, Cassie−Wenzel transformations, triggered by an increase in concentration and decrease in droplet volume, impose diffusion-related limitations. However, the onset of Cassie−Wenzel transformations, driven by increasing concentration and decreasing droplet volume, presents a limitation due to diffusion constraints. Beyond superhydrophobic surfaces, various approaches have been explored to transcend concentration limits, including temperature control,[8] electrowetting,[7,9−12] and mechanical vibration.[13,14] Nonetheless, the uneven deposition caused by the coffee-ring effect (CRE) remains a challenge. This effect, characterized by ring-like depositions during liquid drying on a solid surface, results from differential evaporation flux between the TCL and the droplet's apex, driving particles toward the periphery.[15] Hydrophobicity has been shown to mitigate the CRE. For instance, Cui et al. observed that the evaporation of gel suspensions containing latex spheres on hydrophobic silica column arrays led to homogeneous, ordered macroscopic colloidal photonic crystals, attributed to the Wenzel state in which the latex spheres form porous gel residuals at the edges.[14] Electrowetting-induced substrate interactions and internal circulations can also yield more concentrated analyte residues.[15] Surface acoustic vibrations have been effective in suppressing the CRE.[16,17] Mampallil et al. demonstrated that acoustic control could alter ring-like self-assemblies into homogeneous disc-like or concentrated spot-like residues.[18] Interactions at the base-particle[19−21] and particle−particle levels[22] have been leveraged for similar purposes. Additional strategies, such as altering liquid properties,[16−18] humidity,[19,20] tilt angle utilization,[21] and temperature modulation,[22] have been shown to be effective. Nevertheless, simultaneously enhancing concentration limits and deposition uniformity remains insufficiently addressed in current research.

In this work, we delved into the ultraenrichment of colloidal particles to decode the complex interplay between interfaces, particles, and evaporation dynamics, with the dual objectives of achieving enhanced concentration efficiency and uniform distribution. Our work centers on the development of a droplet manipulation platform incorporating a superhydrophobic (SH) substrate, thereby facilitating dynamic enrichment within evaporating microdroplets. This platform induces controlled, periodic back-and-forth motion of the droplets. The synergistic effect of the substrate's superhydrophobic nature and the orchestrated movement effectively prevent premature particle adherence to the substrate, thus postponing the Cassie−Wenzel transition compared to static deposition methods. Our investigation encompassed model particles with

https://doi.org/10.1021/acsomega.4c10019
ACS Omega 2025, 10, 6038−6046

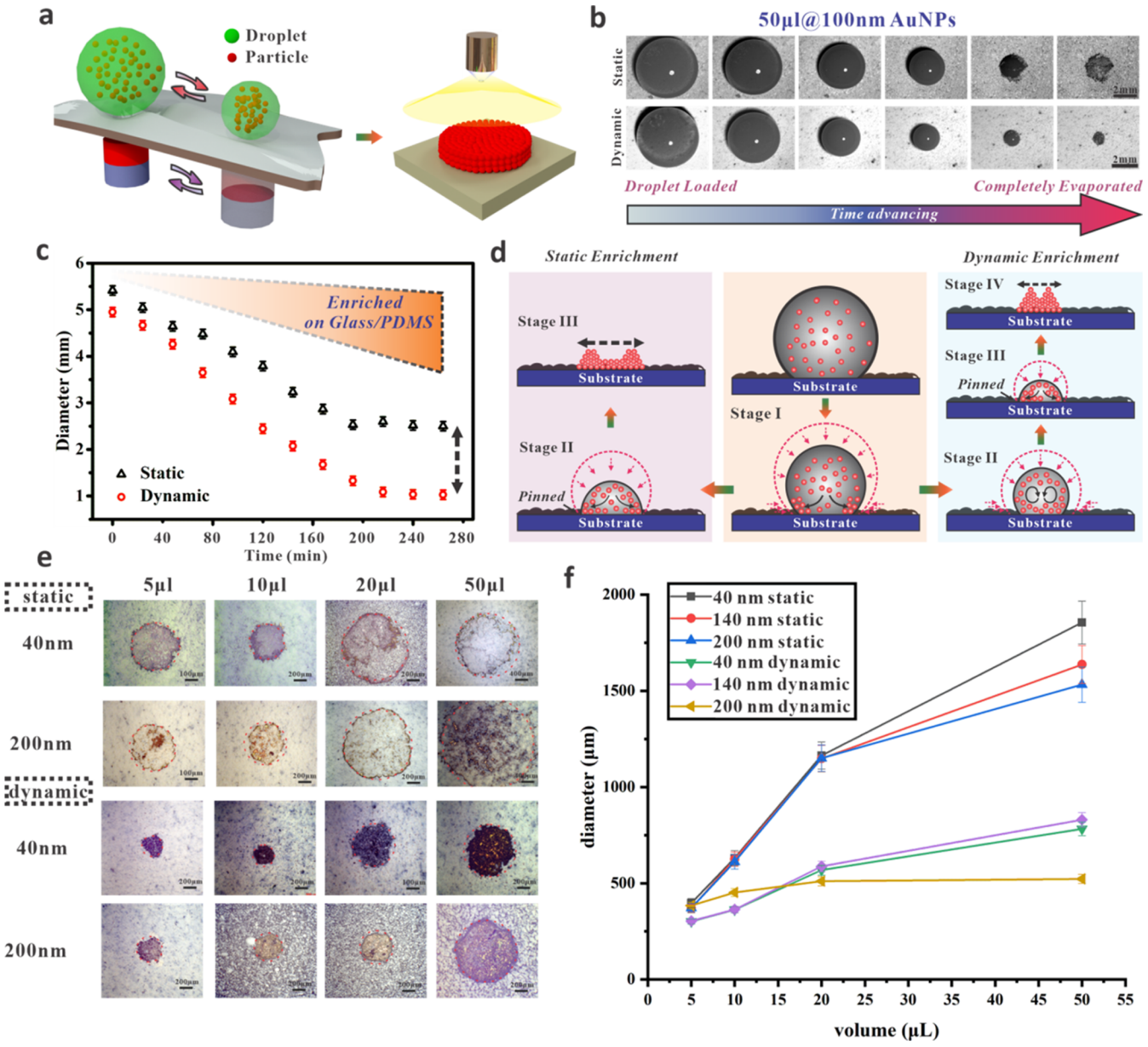

Figure 2. (a) Diagram of dynamic enrichment of droplets containing nanoparticles. (b) Time-lapsed optical images showing the droplet volume variation during the static and dynamic enrichment process. (c) Statistics of static and dynamic droplet diameters in the two types of concentration processes. (d) Diagram of the comparison between the dynamic and static enrichment modes. (e) Optical image of deposition pattern of droplet with different particle size and initial volume for static and dynamic enrichment. (f) Corresponding numerical statistics of diameter of the deposition patterns.

varied densities (polystyrene beads, copper nanoparticles, and gold nanoparticles) and sizes, focusing on their concentrations and drying behaviors on the platform. We conducted a thorough examination and documentation of these behaviors, drawing comparisons to static concentration processes on substrates with different wettability profiles. A notable contribution of our study is the introduction of the "cutoff volume" concept, a pivotal factor in the dynamic concentration process that inversely relates to particle size and ultimately dictates the size of the final deposition pattern. It revealed that our platform not only challenges but also transcends the conventional concentration limits associated with superhydrophobic surfaces while maintaining deposition uniformity. The demonstrated working range of particle properties suggests potential applications for the enrichment of various colloidal systems, which is promising in generating uniform and efficient concentration patterns, especially for analytes present in low concentrations.

2. EXPERIMENTAL SECTION

2.1. Materials. The PDMS precursors (Sylgard 184) and curing agent were obtained from Dow Corning. The commercial hydrophobic silica nanoparticles with an average size of ~40 nm was purchased from Alfa Aesar, to prepare the superhydrophobic coating suspension. Cyclohexane (Damao Chemical Reagent Factory, Tianjin, China) was introduced to dissolve the mixture of PDMS with the silica nanoparticle suspension for surface modification of the PDMS film. Carbonyl iron particles (CIP) were purchased from Sigma-Aldrich to prepare the magnetically functionalized PDMS film.

https://doi.org/10.1021/acsomega.4c10019
ACS Omega 2025, 10, 6038−6046

For the nanoparticles with different densities, the gold nanoparticles (AuNPs) with density of 1.3E + 10 mL^{-1} and diameter of ~40 ± 10 nm, 140 ± 10, and 200 ± 10 nm were purchased from Nanoseedz Ltd., Hong Kong. Copper nanoparticles (99.9%) were purchased from Aladdin Chemical Reagent Co., China. The carboxylate-modified polystyrene microspheres (1 μm, red, 2% solids) were purchased from FluoSpheres.

2.2. Preparation of the Magnetic and Superhydrophobic Film. To start with, a CIP/PDMS composite film was spin-coated (900 rpm for 20 s) onto a clean glass substrate with dimension of 5 cm × 5 cm. A curing process under 150 °C was then carried out for 20 min to ensure complete solidification of the film. Followed with that the superhydrophobic coating was formed onto the substrate by an air brush with constant pressure supply through the nozzle of 0.3 mm with a distance of 10 cm between the brush and the substrate. The homogeneous mixture was prepared with 0.4 g of hydrophobic silica nanoparticles, 0.1 g of PDMS, 0.01 g of curing agent, and 20 mL of cyclohexane. The above mixture was stirred magnetically at about 400 rpm for 60 min before use. A final curing process (80 °C for 1 h) was performed to conclude the fabrication process and realize the superhydrophobic surface for further experiment.

2.3. Characterization and Measurements. The SEM images were captured by scanning electron microscopy (SEM, Sigma FE-SEM, Zeiss Corporation, Germany). All samples were coated with 30 nm platinum before the observation. The contact angle and sliding angle of different substrates were measured with a digital microscope (OSA100S-T, Ningbo NB Scientific Instruments Co. Ltd., Zhejiang, China) at room temperature. All suspensions of nanoparticles were ultrasonicated (power of 300 W and duration of 3 min) to ensure homogeneity before loading to the substrate.

3. RESULTS AND DISCUSSIONS

3.1. Dynamic Enrichment Based on Superhydrophobic and Magnetic Platform. Figure 1a illustrates a schematic diagram of droplet manipulation utilizing a magnetic field to induce localized deformation in a superhydrophobic film. The setup includes a permanent NdFeB cylindrical magnet, 4 mm in diameter with a surface flux of 200 mT, positioned beneath a magnetic and flexible superhydrophobic film measuring 5 cm × 5 cm (shown in Figure 1b). This film, uniformly coated with silica nanoparticles, achieves a superhydrophobic state with a contact angle of 167° and a sliding angle of 2°, as depicted in Figure 1c. Optical images (Figure 1d,e) demonstrate that a localized indentation is created by the magnetic force from the permanent magnet, facilitating precise droplet positioning. The concavity on the surface, resulting from the magnetic components integrated into the film, is detailed in the preparation process (Figure S1). Figure S2 presents the composite gel of carbonyl iron particles (CIP) and PDMS, with CIPs averaging 500 nm to 3 μm in diameter, as evidenced in the SEM images. When a 50 μL droplet is placed on the film, the resultant depression angle, θ, is approximately 12.4°. This angle emerges from the combined effects of droplet gravity and the magnetic force exerted by the external magnetic field, substantially exceeding the roll-off angle of the prepared superhydrophobic film. Figure 1f outlines the fundamental working mechanism for droplet manipulation during evaporation, primarily influenced by the film's minimal roll-off angle and the droplet's gravity. Since the concave angle surpasses the sliding angle, the droplet maintains mobility over an extended period, propelled by a programmable magnet. By employing a permanent magnet attached to an external mechanical arm, the droplet's movement can be precisely controlled, enabling a back-and-forth motion in sync with the underlying magnet (Figure 1g). Additionally, the motion's periodicity is well-defined, as established in our prior research.[23] The cessation of droplet movement during the concentration process is contingent upon alterations in the droplet's gravity and surface adhesion.[24]

We denote the evaporation process of liquid droplets based on the above principle as "dynamic concentration" (Figure 2a). This is contrasted with the "static concentration" process, conducted on identically prepared superhydrophobic surfaces for comparison purposes, as shown in Figure 2b. The key distinction lies in the movement of the droplets: in dynamic concentration, the droplets are subjected to a controlled, periodic motion, whereas in static concentration, the droplets remain stationary throughout the process. This difference is pivotal, as evidenced by the photographs capturing various stages of both static and dynamic concentration processes.[25] It is evident that for droplets of equal initial concentration and volume (50 μL), the dynamic concentration technique results in significantly smaller deposition patterns with a notably more uniform distribution of particles. Statistical analysis (Figure 2c) demonstrates that dynamic concentration patterns occupy merely 16% of the area produced by the static concentration upon complete solvent evaporation. This dramatic improvement in pattern size reduction and uniformity stems from the dynamic approach's effectiveness in preventing particle pinning and accumulation typically induced by capillary-flow and gravitational forces in static conditions. Both processes initially follow the Cassie−Baxter state, where the droplets maintain a constant contact angle, before transitioning to the Wenzel state as they collapse into the rough surface structure.[26,27] The subsequent phase involves a constant contact line with further solvent evaporation leading to a decreasing contact angle while maintaining a fixed diameter. The dynamic concentration method distinctively minimizes contact line binding at the droplet edge, a common limitation in static concentration due to particle accumulation near the periphery, as illustrated in Figure 2d. Throughout these processes, it is important to note that the "diameter" measurements discussed encompass two distinct aspects: the diameter of the liquid droplet during the evaporation process and the diameter of the resultant particle deposition pattern after complete evaporation. The final deposition pattern forms when the suspended nanoparticles settle through the combined effects of capillary-flow and gravitational forces, providing a quantifiable measure to evaluate the effectiveness of different concentration methods.

Consequently, dynamic concentration not only reduces the tendency for particle accumulation but also results in smaller deposition patterns as the controlled movement prevents continuous particle deposition onto the substrate. Consequently, nanoparticles enriched through dynamic concentration are deposited on the superhydrophobic surface with a significantly smaller diameter compared with static concentration. Figure 2e provides optical images of AuNP deposition patterns under both concentration modes, highlighting differences across various particle sizes (40, 140, and 200 nm) and droplet volumes (5, 10, 20, and 50 μL, with additional 100 nm patterns in Figure S3). Statistically, the pattern diameters from dynamic concentration are consistently smaller than those

https://doi.org/10.1021/acsomega.4c10019
ACS Omega 2025, 10, 6038−6046

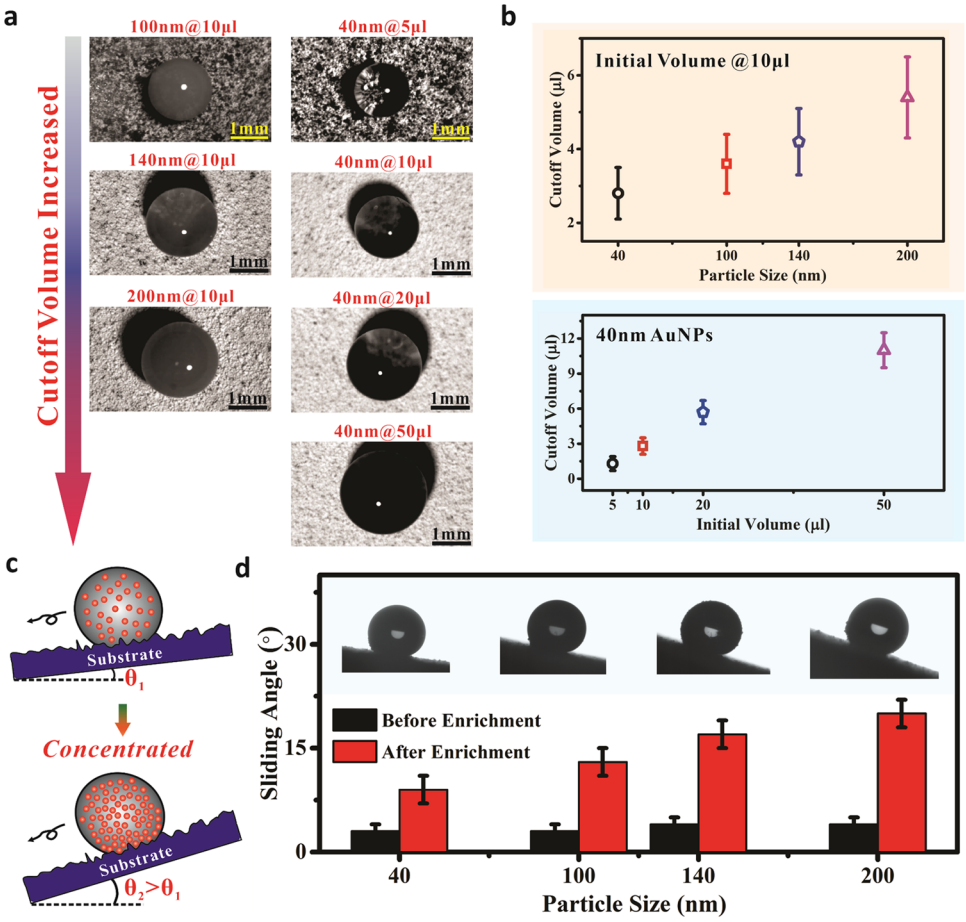

Figure 3. (a) Optical images of cutoff volume for droplet with different initial volumes and particle sizes. Corresponding numerical statistics of cutoff volume are plotted in of in (b). (c) Schematic diagram of the sliding angle of the droplets increases after concentration. (d) Statistics of sliding angles of droplet in cutoff volume.

from static concentration, particularly when dealing with larger initial droplet volumes. Statistical analysis (Figure 2f) reveals that for 50 μL droplets dynamic concentration achieves a 75% reduction in the pattern area across all investigated particle sizes, highlighting its particular effectiveness in producing compact, uniform deposits from larger volume droplets.

3.2. Enrichment Behaviors of Dynamic and Static Modes. The statistical analysis of the dynamic concentration (Figure 2f) reveals a positive correlation between initial droplet volumes and final deposition pattern sizes. This phenomenon can be explained by introducing the concept of "cutoff volume," that is a critical parameter in dynamic enrichment representing the minimum volume below which droplet manipulation becomes impossible on the platform. Figure 3a illustrates optical images of droplets at their respective cutoff volumes for various nanoparticle sizes and initial volumes. The presence of the cutoff volume emerges due to two factors: reduced gravitational effects and increased viscosity during solvent evaporation, ultimately leading to droplet pinning. The cutoff volume exhibits a positive correlation with nanoparticle size, increasing from 3.4 to 5.6 μL as particle diameter increases from 40 to 200 nm (Figure 3b). This correlation can be attributed to particle size effects on suspension properties, specifically increased viscosity and enhanced particle deposition tendencies during evaporation. For 40 nm AuNP suspensions, the cutoff volume variation becomes more pronounced with different initial volumes. Larger initial volumes result in higher particle concentrations per unit volume at the cutoff point, leading to increased droplet viscosity. This manifests as larger sliding angles on the superhydrophobic surface. Consequently, the relationship between droplet manipulation and surface interactions is further evidenced by the inclining angle requirements (Figure 3c). A comparative analysis of rolling-off angles and contact angles before and after concentration for different particle sizes with identical initial volumes (10 μL) supports our hypothesis (Figures 3d and S4). The initial volume significantly influences the rolling-off angle, with supplementary data (Figure S5) showing that even 40 nm particles approach complete pinning (sliding angle ≈90°) when the droplet can no longer be manipulated on the platform. For smaller initial volumes, the pattern area demonstrates proportionality to particle size, consistent with cutoff volume behavior. This relationship emerges because larger nanoparticles under equivalent density conditions exert greater gravitational forces. When droplets reach their cutoff volume and become stationary, gravitational effects dominate over capillary flow during evaporation. Consequently, smaller initial volumes produce larger patterns with increasing particle size and vice versa. This phenomenon can also be understood through the lens of evaporation and internal flow dynamics. As reported by Shen et al.,[28] coffee-ring formation diminishes when solvent evaporation rates exceed particle movement velocities within the droplet. Above certain particle concentration thresholds, capillary-flow-induced par-

https://doi.org/10.1021/acsomega.4c10019
ACS Omega 2025, 10, 6038−6046

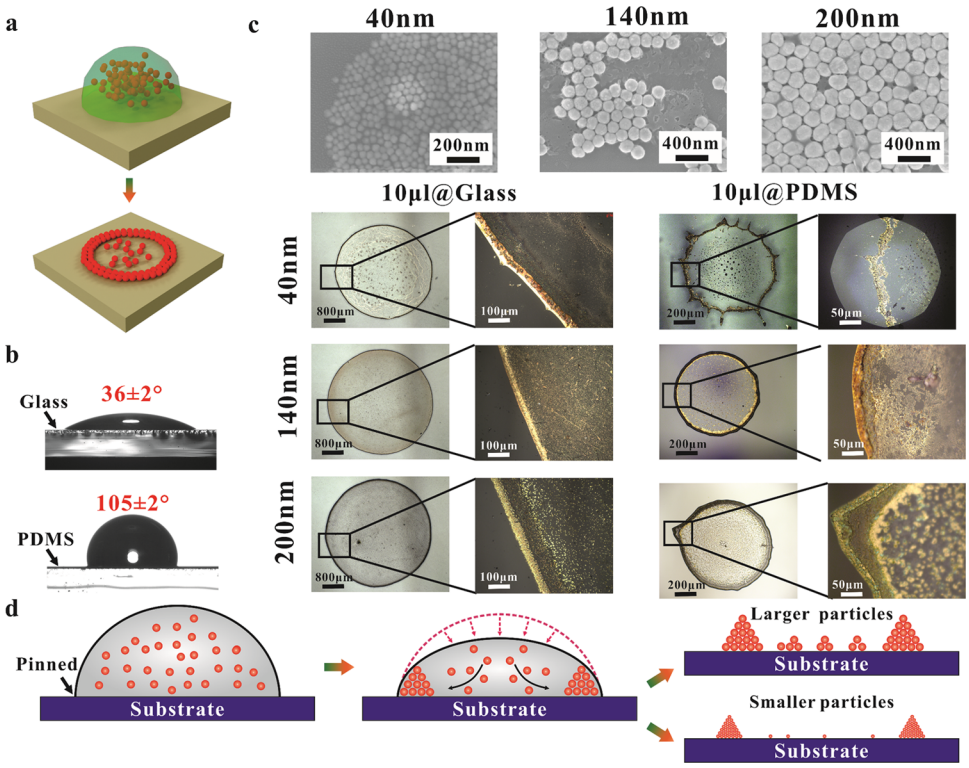

Figure 4. (a) Schematic diagram of static enrichment process. (b) Contact angle of droplet on glass and PDMS substrate. (c) SEM images of AuNPs with different particle sizes and corresponding optical images of 10 μL droplet on glass substrate and PDMS substrate. (d) Schematic diagram showing the enrichment process for nanoparticles with larger and smaller particle sizes.

ticle velocity becomes negligible compared to diffusion velocity. However, for larger initial droplet volumes, the observed phenomenon is more similar to the process of static concentration. It can be assumed that after reaching the cutoff volume soon, further evaporation mainly takes place in the form of constant contact line mode, which is similar to the behavior at high contact angle hysteresis (CAH) surfaces.[29] The deposition behavior of the CAH surface nanoparticles was used to validate the deposition behavior of the following hydrophilic surface (glass, CA of 36°) as well as the hydrophobic PDMS surface.

Figure 4a illustrates the universal deposition process of droplets on nonsuperhydrophobic surfaces. The differential evaporation rates between the droplet's center and edge generate capillary flows that transport nanoparticles toward the periphery, resulting in the characteristic coffee-ring effect. Unlike the spherical cap geometry observed on superhydrophobic surfaces, droplets on these surfaces exhibit greater spreading and larger contact areas (Figure 4b). The surface wettability contrast is evident in the contact angles: 36° ± 2° for glass (hydrophilic) versus 105° for PDMS (hydrophobic), with hydrophilic surfaces consequently producing larger deposition patterns for equivalent droplet volumes. Comparative analysis of deposition patterns across different surface properties (Glass and PDMS film; Figure S6) reveals that pattern diameter reduction becomes more pronounced with increasing hydrophobicity. This effect is particularly evident with larger initial droplet volumes, where the hydrophilic interface promotes a greater pattern expansion. The influence of particle size on deposition behavior is demonstrated in Figure 4c, using 40, 140, and 200 nm AuNPs with 10 μL initial volumes. Smaller particles consistently produce larger deposition patterns. Detailed examination of the deposition patterns through SEM and optical imaging (Figure S6) also reveals distinct particle distribution characteristics in both the ring and central regions. Figure 4d shows that smaller particles preferentially accumulate in the ring region due to their lower mass, making them more susceptible to capillary flow transport and their superior filling capacity during the final evaporation stages when contact angles are minimal. Conversely, larger particles show a greater tendency to aggregate and settle across the substrate without significant ring formation, primarily due to gravitational effects. This particle size-dependent behavior is particularly pronounced on hydrophilic substrates like glass. Consequently, smaller particles predominantly accumulate at the contact line, while larger particles achieve more uniform distribution across the inner region of the pattern. These observations demonstrate the complex interplay between particle size, surface wettability, and deposition mechanics in determining final pattern characteristics.

3.3. Investigation of Nanoparticle Enrichment with Different Densities. In the dynamic concentration process, we investigated particles with varying densities, all of which showed a positive response to the dynamic enrichment despite their different physical properties. Polystyrene beads (0.96−1.04 g/cm^3), copper nanoparticles (8.96 g/cm^3), and gold nanoparticles (19.32 g/cm^3), as the dispersed particles, were selected herein for comparison with the identical diameter of ∼140 nm. These particles were stabilized by carboxylate modification, polyvinylpyrrolidone (PVP), and CTAB respectively, though these stabilizing agents showed minimal influence on the enrichment process. Figure 5 presents the deposition patterns and corresponding statistical

https://doi.org/10.1021/acsomega.4c10019
ACS Omega 2025, 10, 6038−6046

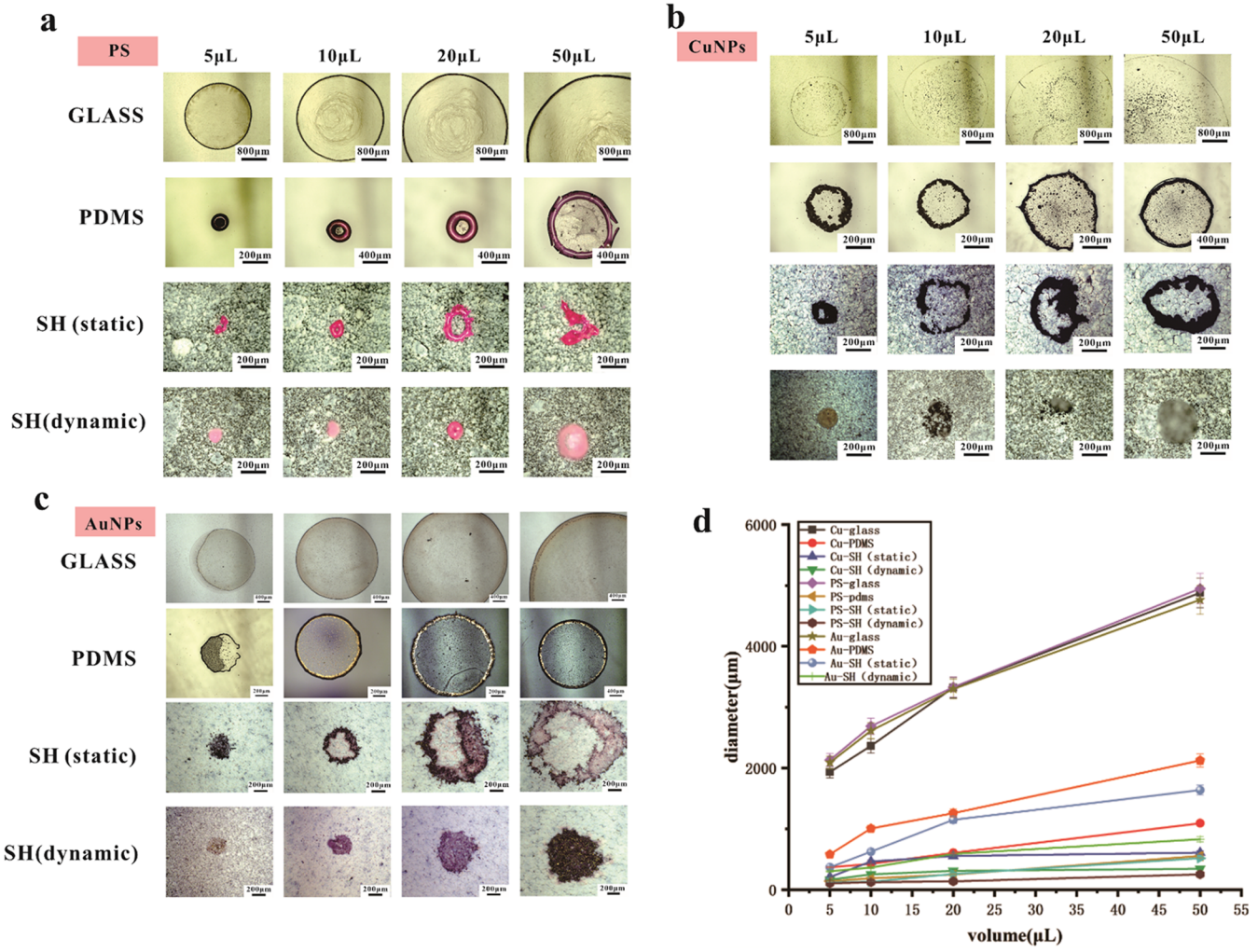

Figure 5. Optical images and numerical statistics of drying deposit of droplet with different particle densities and same particle size of ∼140 nm in diameter. (a) Polystyrene beads. (b) Copper nanoparticles. (c) Gold nanoparticles. (d) Statistics of diameter of the deposition patterns from different particles on various substrates.

data for both static and dynamic enrichment across various initial droplet volumes on glass, PDMS, and superhydrophobic surfaces. Surface properties of the substrate demonstrate a critical influence on the deposition pattern diameter. (Figure 5a−d) Through systematic comparisons across different surfaces, we observe that dynamic enrichment leads to not only significantly reduced pattern sizes but also more uniform particle distribution compared to static conditions. For high-density particles (Au and Cu nanoparticles), the interplay between capillary forces and gravitational effects during the constant contact line phase results in notably uniform deposition patterns without obvious ring formation. For lighter PS microspheres in Figure 5a, while ring-like regions are still observable due to their lower susceptibility to gravitational settling, the dynamic enrichment process achieves significantly smaller pattern sizes with relatively uniform thickness between the center and peripheral regions. This difference in deposition uniformity becomes particularly evident when comparing the color contrast of patterns across different surfaces, from hydrophilic glass to hydrophobic PDMS and superhydrophobic PDMS-silica surfaces, where the coffee-ring effect gradually diminishes, with dynamic enrichment on superhydrophobic surfaces exhibiting the most consistent coloration across the pattern area. The effectiveness of our platform is further demonstrated by the consistent performance across different particle densities, where deposition pattern areas decrease significantly through dynamic enrichment (Figures 5b,c and S7). For the analyzed particles, SEM analysis of the substrate areas outside the final deposition patterns shows a negligible particle presence (Figure S8), indicating minimal material loss during the dynamic enrichment process. This self-cleaning property of the superhydrophobic surface effectively prevents particle adhesion during droplet movement, ensuring efficient particle collection in the final deposition pattern. However, for particles with larger size, the intrinsic gravity will dominate the motion within the droplet when compared with the capillary flow. Consequently, the larger AuNPs will tend to deposit onto the substrate before they are dragged to the contact line via capillary flow. This phenomenon is exemplified by 500 nm AuNPs (Figure S9), where static enrichment of a 10 μL droplet shows a minimal coffee-ring effect, with nanoparticles depositing uniformly within the pattern area. Although heavier nanoparticles settle before reaching the cutoff volume during dynamic concentration, the overall deposition pattern area remains significantly reduced, confirming the effectiveness of dynamic enrichment for larger particles.

For some typical bio/chemical analyses, the initial concentration is typically low, and thus, the enrichment is

https://doi.org/10.1021/acsomega.4c10019
ACS Omega 2025, 10, 6038−6046

highly appreciated before the analysis.[24,30,31] Notably, the density range of common biological particles primarily falls within 0.9944−2.635 g/cm^3, which closely aligns with the density range of particles utilized in our experiments. Particularly, this range is remarkably similar to that of the polystyrene microspheres (0.96−1.04 g/cm^3)), which demonstrated optimal performance in our study. This density congruence strongly suggests the high feasibility of applying this method in biological contexts. Furthermore, the particle sizes of most biological entities are predominantly in the nano- and micrometer range, closely matching the dimensions of the particles employed in our experiments. This size similarity further corroborates the aforementioned assertion regarding the method's biological applicability. The correspondence of these characteristics provides a solid foundation for extending this technique to the analysis and enrichment of various biological samples (Tables S1 and S2). Besides, the dynamic nature of our platform may provide additional advantages for biological sample analysis. The continuous movement prevents surface-active species from accumulating at interfaces, which is a common limitation in static systems. Besides, the dynamic nature of our platform offers unique advantages through continuous reorganization of the water−air interface. This constant motion prevents surface pinning and maintains fresh interfacial areas, which could potentially enhance interface-mediated reactions by preventing product inhibition and ensuring a uniform concentration distribution. Such interface renewal effects, previously observed in "on-water" catalysis systems, suggest promising applications beyond simple enrichment.[32]

Given the possibility of dynamic enrichment under a large initial volume, we finally used diluted targets with different ratios and investigated the capability of enrichment based on the dynamic platform. Using AuNPs (40 nm) as an example, we diluted the 5 μL droplets to 10 μL (2 times), 20 μL (4 times), and 50 μL (10 times) to compare the performance based on dynamic and static enrichments. Besides, as shown in Figure S10, the dynamically concentrated pattern clearly has a smaller deposition area of the AuNPs when compared with the static mode. We also notice that with a larger initial droplet volume (higher dilution ratio), the deposition pattern is relatively larger even under the dynamic enrichment mode, which was possibly induced by the longer evaporation duration and the continuous gravity-induced deposition of the AuNPs across the trajectory. Overall, the results herein reveal that the continuous movement of the droplets can effectively enrich the targets with broad application diversity.

4. CONCLUSIONS

Influenced by the designed magnetic driven superhydrophobic platform, the concentration behavior of the droplets is simultaneously influenced by the two factors of mechanical disturbance and surface energy. Therefore, after the dispersion medium is completely evaporated, it presents a disperse phase pattern that breaks the traditional concentration limit.

In this work, the dynamic concentration based on the designed platform is considered to break the existing concentration limit and contribute to the suppression of the coffee ring. Furthermore, the concept of cutoff volume was introduced to better segment and define the different stages of the complete enrichment process. In this way, the whole process can be simplified into two stages that are different from the conventional static enrichment. The dynamic enrichment can obviously reduce the deposition pattern area thanks to the capability of "depinning" effect, which allows the droplet to be concentrated into an ultrasmall area. Finally, we systematically investigated the behavior of the droplet dried pattern formation regarding the initial droplet volumes, nanoparticle sizes, densities, etc. in both static and dynamic mode. The results experimentally presented that the platform has varying degrees of promotion for almost all variable droplets in terms of concentration efficiency and uniformity. The synergistic concentration effect of mechanical disturbance-liquid-repellent surface platform has thus been proved to have universal applicability, with great application potential in environmental pollution management, food safety, and biomedicine. This result will also provide a reference for quality design in actual application scenarios and effectively improve the detection efficiency of low-concentration samples.

■ ASSOCIATED CONTENT

Data Availability Statement

The data underlying this study are available in the published article and its Supporting Information

Supporting Information

The Supporting Information is available free of charge at https://pubs.acs.org/doi/10.1021/acsomega.4c10019.

Fabrication details of magnetic-superhydrophobic film and CIP/PDMS composite characterization (Figures S1 and S2); deposition patterns under different conditions (Figures S3−S5, S7, S9 and S10); contact angle measurements (Figure S6); SEM-EDS analysis of nondeposition areas (Figure S8); and biological particle properties (Tables S1 and S2) (PDF)

■ AUTHOR INFORMATION

Corresponding Authors

Ziyi Dai − *School of Integrated Circuits, Shandong University, Jinan 250100, China;* orcid.org/0000-0002-2749-2872; Email: ziyidai@sdu.edu.cn

Kai Qian − *School of Integrated Circuits, Shandong University, Jinan 250100, China;* orcid.org/0000-0002-4049-4426; Email: kaiqian@sdu.edu.cn

Authors

Tianyi Lu − *State Key Lab of Environmental Adaptability for Industrial Products, Guangzhou 510275, China*

Miaoran Liu − *State Key Lab of Environmental Adaptability for Industrial Products, Guangzhou 510275, China*

Yifei Xiao − *School of Integrated Circuits, Shandong University, Jinan 250100, China*

Yimeng Xu − *School of Integrated Circuits, Shandong University, Jinan 250100, China*

Yu Wang − *School of Integrated Circuits, Shandong University, Jinan 250100, China*

Complete contact information is available at: https://pubs.acs.org/10.1021/acsomega.4c10019

Author Contributions

§T.L., M.L., and Y.X. contributed equally to this work.

Notes

The authors declare no competing financial interest.

https://doi.org/10.1021/acsomega.4c10019
ACS Omega 2025, 10, 6038−6046

■ ACKNOWLEDGMENTS

The authors appreciate the supported by the State Key Lab of Environmental Adaptability for Industrial Products (Project No.2024EASKJ-002).

■ REFERENCES

(1) De Angelis, F.; Gentile, F.; Mecarini, F.; Das, G.; Moretti, M.; Candeloro, P.; Coluccio, M. L.; Cojoc, G.; Accardo, A.; Liberale, C.; Zaccaria, R. P.; Perozziello, G.; Tirinato, L.; Toma, A.; Cuda, G.; Cingolani, R.; Fabrizio, E. D. Breaking the diffusion limit with super-hydrophobic delivery of molecules to plasmonic nanofocusing SERS structures. *Nat. Photonics* **2011**, *5*, 682−687.

(2) Wallace, R. A.; Charlton, J. J.; Kirchner, T. B.; Lavrik, N. V.; Datskos, P. G.; Sepaniak, M. J. Superhydrophobic analyte concentration utilizing colloid-pillar array SERS substrates. *Anal. Chem.* **2014**, *86*, 11819−11825.

(3) Guo, J.; Liang, Z.; Huang, Y.; Kim, K.; Vandeventer, P.; Fan, D. Acceleration of Biomolecule Enrichment and Detection with Rotationally Motorized Opto-Plasmonic Microsensors and the Working Mechanism. *ACS Nano* **2020**, *14*, 15204−15215.

(4) Lv, H.; Guan, Q.; Wang, Y.; Zhang, X. Low-dimensional material based wearable sensors. *RSC Adv.* **2021**, *11*, 12893−12901.

(5) Xu, J.; Si, Y.; Li, Z.; Jiang, S.; Xiu, X.; Lei, F.; Du, F. X.; Du, X.; Man, B.; Man, B.; Yu, J.; Yu, J.; Zhang, C. Multiscale structure enabled effective plasmon coupling and molecular enriching for SERS detection. *Appl. Surf. Sci.* **2021**, *544*, No. 148908.

(6) Singh, S. K.; Gogna, M.; Khandekar, S.; Muralidhar, K.Evaporation Dynamics of a Sessile Droplet on a Hydrophobic Surface. In *Drop Dynamics and Dropwise Condensation on Textured Surfaces*; Springer, 2020; pp 395−410.

(7) Boreyko, J. B.; Collier, C. P. Dewetting transitions on superhydrophobic surfaces: When are Wenzel drops reversible? *J. Phys. Chem. C* **2013**, *117*, 18084−18090.

(8) Kumari, N.; Garimella, S. V. Electrowetting-induced dewetting transitions on superhydrophobic surfaces. *Langmuir* **2011**, *27*, 10342−10346.

(9) Lapierre, F.; Coffinier, Y.; Boukherroub, R.; Thomy, V. Electro-(de) wetting on superhydrophobic surfaces. *Langmuir* **2013**, *29*, 13346−13351.

(10) Boreyko, J. B.; Collier, C. P. Delayed Frost Growth on Jumping-Drop Superhydrophobic Surfaces. *ACS Nano* **2013**, *7*, 18084−18090.

(11) Mampallil, D.; Eral, H.; Van Den Ende, D.; Mugele, F. Control of evaporating complex fluids through electrowetting. *Soft Matter* **2012**, *8*, 10614−10617.

(12) Cui, L.; Zhang, J.; Zhang, X.; Li, Y.; Wang, Z.; Gao, H.; Wang, T.; Zhu, S.; Yu, H.; Yang, B. Avoiding coffee ring structure based on hydrophobic silicon pillar arrays during single-drop evaporation. *Soft Matter* **2012**, *8*, 10448−10456.

(13) Deegan, R. D.; Bakajin, O.; Dupont, T. F.; Huber, G.; Nagel, S. R.; Witten, T. A. Capillary Flow as the Cause of Ring Stains From Dried Liquid Drops. *Nature* **1997**, *389*, 827−829.

(14) Mampallil, D.; Eral, H. B. A review on suppression and utilization of the coffee-ring effect. *Adv. Colloid Interface Sci.* **2018**, *252*, 38−54.

(15) Wray, A. W.; Papageorgiou, D. T.; Craster, R. V.; Sefiane, K.; Matar, O. K. Electrostatic Suppression of the "Coffee Stain Effect. *Langmuir* **2014**, *30*, 5849−5858.

(16) Ji, B.; Zhang, L.; Li, M.; Wang, S.; Law, M.-K.; Huang, Y.; Wen, W.; Zhou, B. Suppression of coffee-ring effect via periodic oscillation of substrate for ultra-sensitive enrichment towards surface-enhanced Raman scattering. *Nanoscale* **2019**, *11*, 20534−20545.

(17) Muangnapoh, T.; Weldon, A. L.; Gilchrist, J. F. Enhanced colloidal monolayer assembly via vibration-assisted convective deposition. *Appl. Phys. Lett.* **2013**, *103*, No. 181603.

(18) Mampallil, D.; Reboud, J.; Wilson, R.; Wylie, D.; Klug, D. R.; Cooper, J. M. Acoustic suppression of the coffee-ring effect. *Soft Matter* **2015**, *11*, 7207−7213.

(19) Crivoi, A.; Duan, F. Elimination of the coffee-ring effect by promoting particle adsorption and long-range interaction. *Langmuir* **2013**, *29*, 12067−12074.

(20) Crivoi, A.; Zhong, X.; Duan, F. Crossover from the coffee-ring effect to the uniform deposit caused by irreversible cluster-cluster aggregation. *Phys. Rev. E* **2015**, *92*, No. 032302.

(21) Dugyala, V. R.; Basavara, M. G. Control over coffee-ring formation in evaporating liquid drops containing ellipsoids. *Langmuir* **2014**, *30*, 8680−8686.

(22) Crivoi, A.; Duan, F. Amplifying and attenuating the coffee-ring effect in drying sessile nanofluid droplets. *Phys. Rev. E* **2013**, *87*, No. 042303.

(23) Soltman, D.; Subramanian, V. Inkjet-Printed Line Morphologies and Temperature Control of the Coffee Ring Effect. *Langmuir* **2008**, *24*, 2224−2231.

(24) Du, X.; Deegan, R. Ring formation on an inclined surface. *J. Fluid Mech.* **2015**, *775*, No. R3, DOI: 10.1017/jfm.2015.312.

(25) Chen, G.; Ji, B.; Gao, Y.; Wang, C.; Wu, J.; Zhou, B.; Wen, W. Towards the rapid and efficient mixing on'open-surface'droplet-based microfluidics via magnetic actuation. *Sens. Actuators, B* **2019**, *286*, 181−190.

(26) Shen, X.; Ho, C.-M.; Wong, T.-S. Minimal size of coffee ring structure. *J. Phys. Chem. B* **2010**, *114*, 5269−5274.

(27) Li, N.; Wu, D.; Hu, N.; Fan, G.; Li, X.; Sun, J.; Chen, X.; Suo, Y.; Li, G.; Wu, Y. Effective enrichment and detection of trace polycyclic aromatic hydrocarbons in food samples based on magnetic covalent organic framework hybrid microspheres. *J. Agric. Food Chem.* **2018**, *66*, 3572−3580.

(28) Talbot, E. L.; Yow, H. N.; Yang, L.; Berson, Al.; Biggs, S. R.; Bain, C. D. Printing Small Dots from Large Drops. *ACS Appl. Mater. Interfaces* **2015**, *7*, 3782−3790.

(29) Ji, J.; Nie, L.; Li, Y.; Yang, P.; Liu, B. Simultaneous online enrichment and identification of trace species based on microfluidic droplets. *Anal. Chem.* **2013**, *85*, 9617−9622.

(30) Msambwa, Y.; Shackleford, A.; Ouali, F.; Fairhurst, D. Controlling and characterising the deposits from polymer droplets containing microparticles and salt. *Eur. Phys. J. E* **2016**, *39*, 1−8.

(31) Kajiya, T.; Kobayashi, W.; Okuzono, T.; Doi, M. Controlling the drying and film formation processes of polymer solution droplets with addition of small amount of surfactants. *Langmuir* **2010**, *26*, 10429−10432.

(32) Mellouli, S.; Bousekkine, L.; Theberge, A. B.; Huck, W. T. Investigation of "On Water" Conditions Using a Biphasic Fluidic Platform. *Angew. Chem., Int. Ed.* **2012**, *51*, 7981−7984.

https://doi.org/10.1021/acsomega.4c10019
ACS Omega 2025, 10, 6038−6046